Deployment of a Tethered-Balloon System for Microphysics and Radiative Measurements in Mixed-Phase Clouds at Ny-Ålesund and South Pole

R. PAUL LAWSON,* KNUT STAMNES,+ JAKOB STAMNES,# PAT ZMARZLY,* JEFF KOSKULIKS,+ CHRIS RODEN,* QIXU MO,* MICHAEL CARRITHERS,* AND GEOFFREY L. BLAND@

* *SPEC, Inc., Boulder, Colorado*
+ *Stevens Institute of Technology, Hoboken, New Jersey*
# *University of Bergen, Bergen, Norway*
@ *Wallops Flight Facility, NASA Goddard Space Flight Center, Greenbelt, Maryland*

(Manuscript received 6 June 2010, in final form 20 September 2010)

ABSTRACT

A tethered-balloon system capable of making microphysical and radiative measurements in clouds is described and examples of measurements in boundary layer stratus clouds in the Arctic and at the South Pole are presented. A 43-m^3 helium-filled balloon lofts an instrument package that is powered by two copper conductors in the tether. The instrument package can support several instruments, including, but not limited to, a cloud particle imager; a forward-scattering spectrometer probe; temperature, pressure, humidity, and wind sensors; ice nuclei filters; and a 4-π radiometer that measures actinic flux at 500 and 800 nm. The balloon can stay aloft for an extended period of time (in excess of 24 h) and conduct vertical profiles up to about 1–2 km, contingent upon payload weight, wind speed, and surface elevation. Examples of measurements in mixed-phase clouds at Ny-Ålesund, Svalbard (79°N), and at the South Pole are discussed. The stratus clouds at Ny-Ålesund ranged in temperature from 0° to −10°C and were mostly mixed phase with heavily rimed ice particles, even when cloud-top temperatures were warmer than −5°C. Conversely, mixed-phase clouds at the South Pole contained regions with only water drops at temperatures as cold as −32°C and were often composed of pristine ice crystals. The radiative properties of mixed-phase clouds are a critical component of radiative transfer in polar regions, which, in turn, is a lynch pin for climate change on a global scale.

I. Introduction

Climate change appears to be more pronounced in the Arctic than in other regions of the globe (e.g., Holland and Bitz 2003), and it has gradually become clear that the Arctic is much more important for the global climate than had been anticipated. The reasons for this are (i) the most dramatic changes occur in the Arctic (Rothrock et al. 1999; Houghton et al. 2001), and (ii) the high northern latitudes have a disproportionately large influence on the global climate (Meehl and Washington 1990; Alley 1995). Large decreases in sea ice extent and thickness have been observed in recent years (Chapman and Walsh 1993; Vinnikov et al. 1999), and surface temperatures have increased (Chen et al. 2002; Serreze et al. 2000; Stone 1997). Arzel et al. (2006) have shown that climate models indicate a large-scale retreat of sea ice in the Nordic seas with a corresponding increase in the mean wintertime sea surface temperature (SST). An increase in the SST may provide greater moisture fluxes for increased latent heat release, which have been shown to enhance the intensification of arctic fronts and polar lows (Emanuel and Rotunno 1989; Grønås and Skeie 1999). Although future projections from global climate models vary, there is wide agreement that the arctic ice cover will shrink considerably. The Barents Sea and the area around Svalbard are crucial because of feedback mechanisms and the high variability in the sea ice cover.

It is well known now that clouds have a particularly strong nonlinear influence on the surface energy budget in the Arctic (Tsay et al. 1989; Curry and Ebert 1992; Intrieri et al. 2002a; Schweiger and Key 1994; Walsh and Chapman 1998), including the timing of the onset of snowmelt (Zhang et al. 1997). The explanation is straightforward: relatively thin boundary layer clouds that are prolific in spring and through fall in the Arctic (Lawson et al. 2001; Intrieri et al. 2002a,b; Zuidema et al. 2004; Lawson and Zuidema 2009) transmit (shortwave) sunlight and absorb

Corresponding author address: Dr. R. Paul Lawson, Suite 200, 3022 Sterling Circle, SPEC, Inc., Boulder, CO 80301.
E-mail: plawson@specinc.com

DOI: 10.1175/2010JTECHA1439.1

(longwave) thermal radiation. This greenhouse effect produced by the thin cloud cover accelerates melting and increases the amount of open water, which absorbs more incoming sunlight than the ice surfaces, setting up a positive feedback process that leads to more melting and warming near the surface.

The radiative interaction between the atmosphere and the surface (snow–sea ice–ocean) is of paramount importance in the Arctic, where the net radiation is the largest component of the surface energy budget. Also, unlike any other region on the globe, clouds exert a positive net radiative forcing at the surface resulting from a combination of high surface albedo and strong surface inversions (Intrieri et al. 2002b). A proper treatment of clouds in the polar regions is a prerequisite for reliable estimates of climate forcing, the onset of snowmelt, the rate of snow/ice ablation, the length of the melt season (Zhang et al. 1997) and, ultimately, the fate of sea ice and ice sheets in a changing climate.

Global climate models (GCMs) are very sensitive to the radiative effects of clouds. Walsh et al. (2005), summarizing the results of a workshop on the ability of GCMs to reliably predict arctic climate, state that arctic cloudiness is one of the greatest uncertainties in global model simulations of climate change. They go on to point out that mixed-phase clouds pose special challenges to cloud formulations. Using a GCM that includes the parameterized treatment of mixed-phase microphysics, Vavrus (2004) concluded that the inclusion of mixed-phase microphysics may be essential for realistically simulating the annual cycle of Arctic cloud. Walsh et al. (2005) go on to point out that clouds have often been used as "tuning knobs" in GCMs, and that determining whether models capture the seasonal cycle of Arctic clouds for the right reasons is a high priority. They state that this assessment will need to address the vertical distributions and optical properties of the simulated clouds.

Mixed-phase Arctic boundary layer clouds typically have microphysical properties that are inhomogeneous, often on horizontal and vertical scales of a few kilometers and less. For example, Lawson et al. (2001) analyzed in situ aircraft data in Arctic stratus and found that 11 of 12 clouds with subfreezing temperatures contained supercooled droplets. Lawson and Zuidema (2009) observed that layers of all-water and all-ice clouds can be interspersed with regions of supercooled drizzle and graupel on horizontal scales of a few kilometers. Accurate measurements of mixed-phase clouds are important for assessing cloud optical depth, which is simply the integral of the extinction coefficient over cloud thickness. Supercooled liquid predominantly contributes to the extinction coefficient (Hogan et al. 2003; Sun and Shine 1994) and the surface infrared flux. The ice contribution to the extinction coefficient may be small, but the ice phase regulates the overall optical depth, because the transition to all-ice conditions can be associated with a large drop in the cloud optical depth (Curry and Ebert 1992; Sun and Shine 1994).

A tethered-balloon system (TBS) is capable of making repeated vertical profiles of microphysical and radiative properties of boundary layer stratus clouds in polar regions. By parking the instrument package at a fixed altitude, the time history and an estimate of cloud horizontal structure can be obtained. Most previous balloon-borne cloud physics packages have used small, untethered balloons with either particle replicators or digital cameras that recorded images on oil-coated tape (Heymsfield and Miloshevich 1995; Orikasa and Murakami 1997). One exception is Walden et al. (2005), who used a small tethered balloon and a digital camera system (Orikasa and Murakami 1997) to make limited measurements of the first in situ observations of supercooled water in clouds at the South Pole.

The TBS described in this paper is an outgrowth of a system that was developed in 1997 for the Surface Heat Budget of the Arctic Ocean (SHEBA)/First International Satellite Cloud Climatology Project (ISCCP) Regional Experiment (FIRE) Arctic Cloud Experiment (ACE) project. The previous TBS used a 9-m^{-3} helium-filled balloon and a video camera to record images of cloud particles on oil-coated tape (Borys et al. 1999). The current TBS used a 43-m^{-3} helium-filled balloon and a more sophisticated cloud physics and radiation measurements package. A TBS that supports a sophisticated microphysical and radiative package has both advantages and disadvantages compared with instrumented aircraft.

a. Advantages of a TBS

Advantages of a TBS include the following:

- A TBS can stay aloft and collect microphysical data for extended (>24 h) periods.
- A TBS makes vertical profiles of clouds from about 2 km all the way down to the surface and, unlike aircraft, a TBS covers the full vertical extent of most boundary layer Arctic clouds. Table 2 in Lawson et al. (2001) shows that 8 of the 11 SHEBA/FIRE ACE boundary layer clouds had tops within 2 km of the surface. Depending on horizontal wind speed, a TBS profile is nearly vertical relative to a moving cloud, whereas an aircraft makes either slanted or spiral profiles, which mix regions of clouds over horizontal scales of several kilometers.
- Unlike powered aircraft, a TBS does not disturb the cloud environment and does not artificially create ice

particles, which has been associated with some research aircraft (e.g., Rangno and Hobbs 1983).
- Because of the relatively slow ($\sim$10 m s^{-1}) aspiration speed, TBS microphysical measurements from cloud particle probes will not be subjected to the inadequate time response of the electronics (e.g., Baumgardner and Korolev 1997; Lawson et al. 2006), drop splashing, and ice crystal shattering on probe inlets (e.g., Field et al. 2003; Korolev and Isaac 2005; Baker et al. 2009), all of which have been shown to be problematical at aircraft speeds.
- The cost of operation of a TBS is a small fraction of that required to support a research aircraft in a field campaign.

b. Disadvantages of a TBS

Disadvantages of a TBS include the following:

- A (relatively small) TBS can support only a fraction of the payload of an instrumented aircraft.
- The TBS described here does not function well in moderate winds ($>\sim$10 m s^{-1}). There are balloon and kite systems that are designed for much higher winds (up to 30 m s^{-1}); however, these systems have yet to be utilized for cloud research.
- A TBS can neither make horizontal measurements, nor be repositioned without substantial logistical support.
- Microphysical measurements of cloud particles (e.g., particle size distributions) have yet to be evaluated quantitatively because factors such as particle collection efficiency are not yet well understood.

While there are advantages and disadvantages of TBSs compared with aircraft microphysical measurements, data from each platform can be combined synergistically to build a more comprehensive picture of cloud properties. For example, repeated TBS vertical profiles from cloud base to cloud top can be compared to results from column models with detailed microphysics packages. Aircraft measurements that cover a large spatial area can be integrated with the column model to improve comparisons with simulations of mesoscale cloud systems. Repeated TBS vertical profiles of both cloud microphysical and radiative properties can be used to improve remote retrievals that are made by aircraft flying along the wind vector over the cloud top. The ability of the TBS to conduct fine-resolution vertical profiles in mixed-phase polar clouds can be especially beneficial in improving retrievals using multiple remote sensors, such as cloud radar, polarized lidar, and high spectral radiometers.

This paper describes the instrumentation and sampling characteristics of a TBS (section 2). In section 3, microphysical and radiative measurements collected in mixed-phase Arctic and Antarctic stratus clouds are discussed. Section 4 summarizes results and offers suggestions for continued improvement of TBSs.

2. Description of the TBS

Based on lessons learned from the development of a TBS for the SHEBA/FIRE ACE project, Stratton Park Engineering Company, Inc. (SPEC) was awarded a Small Business Innovation Research (SBIR) grant from the Department of Energy (DOE) to develop an upgraded TBS. The upgraded TBS included a lightweight version of the cloud particle imager (CPI) used on research aircraft (Lawson et al. 2001); a custom-made 4-π radiometer (Stamnes and Storvold 1999); and a meteorology package measuring temperature, pressure, humidity, GPS position, wind speed, and direction. Figure 1 contains photographs of the TBS as it was deployed in Ny-Ålesund, Svalbard, showing the 43-m^3 balloon, microphysics package, 4-π radiometer, winch, and tether. Figure 2 is a schematic diagram showing the basic components of the TBS and instrument package. The main instrument package includes the CPI and computer, fast forward-scattering spectrometer probe (FSSP), and meteorological package (temperature, pressure, GPS position, and wind direction and speed). The cryogenic frost-point hygrometer (Vömel et al. 2007) is attached to a separate compartment at the bottom of the main package, and the 4-π radiometer is attached to the main tether below the package.

The weight of the balloon, tether(s), and rigging must be subtracted to compute the weight of the payload that can be lofted by the balloon. The balloon weighs 16.6 kg (36.5 lb). The primary tether weighs 7.23 kg km^{-1} [4.85 lb (1000 ft)$^{-1}$] and the backup (safety) tether, which is used in parallel with the primary tether, weighs 2.1 kg km^{-1} [1.4l lb (1000 ft)$^{-1}$]. The primary tether has a breaking strength of 580 lb and is a custom design that contains two insulated 24-awg copper wires with ethylene–propylene copolymer insulation, nylon filler, a Vectran strength member, and a braided polyester cover. The backup tether is a plasma braid with a breaking strength of 750 lb. A 1500-Vdc, 3-A power supply powers the instrument package via the copper conductors in the tether. Data are recorded at the instrument package on a flash drive and are also transmitted to the ground using a 5.8-GHz spread spectrum General Mobile Radio Service (GMRS) radio link.

A solid model of the lightweight version of the CPI used in the TBS is shown in Fig. 3. The TBS CPI is very similar to the aircraft version. The main differences between the aircraft and TBS CPIs are as follows:

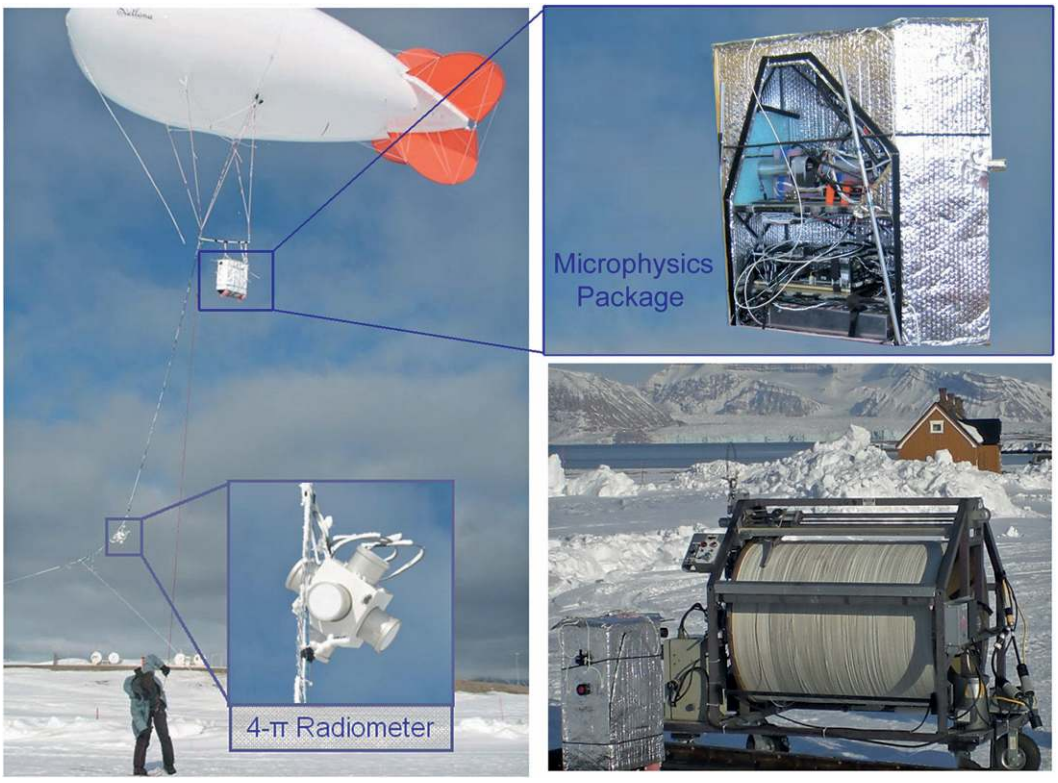

FIG. 1. Photographs showing the tethered-balloon and winch system used to measure cloud microphysical and radiative properties in Svalbard, May/June 2008. The balloon is 43 m^3 and will loft a 15-kg instrument package from sea level to nearly 2 km in calm wind conditions. The custom tether provides continuous power to the package that allows it to operate for extended (>24 h) periods.

1) The TBS CPI does not have a housing required for high-speed application in the aircraft CPI.
2) The TBS CPI has 3-μm pixel resolution and effectively a 480 $\times$ 480 pixel digital camera, compared with 2.3-μm pixel resolution and a 1024 $\times$ 1024 pixel camera found in the aircraft CPI. The maximum particle dimension imaged in the TBS CPI is 1.44 mm, while the maximum particle imaged by the aircraft CPI is 2.36 mm.
3) The TBS CPI does not require a correction plate, which is used in the aircraft CPI to correct for astigmatism caused by the laser passing obliquely through a window in the sample tube; the lack of a correction plate and the much slower transit speed of the particles results in a slightly improved TBS image resolution.[1]

[1] While the aircraft (version 2) CPI has smaller pixels, 2.3 μm compared with 3 μm in the TBS CPI, the aircraft images are subjected to blur caused by an optical correction plate and the high speed of the particles, resulting in an effective image resolution of 4 to 5 μm. The TBS does not need a correction plate and the particle speed is low, resulting in 3-μm image resolution.

The aspiration technique in the TBS uses a miniaturized version of the unit successfully used on the surface at the South Pole (Lawson et al. 2006). The aircraft CPI has been shown to be unique in its ability to distinguish water drops from ice particles, based on the roundness of the images (Lawson et al. 2001; Korolev and Isaac 2003; Baker and Lawson 2006a). Images from the TBS CPI are of the same quality as the aircraft CPI, so that the same roundness algorithms used to discriminate water drops from ice can be applied to TBS CPI data.

The TBS fast FSSP measures the size distribution of particles from 1 to 50 μm and uses optics that are based on the FSSP-300X (Baumgardner et al. 1992). It measures individual particle statistics, similar to, but exceeding, those measured by the fast FSSP described by Brenguier et al. (1998). The TBS fast FSSP records signal and qualifier peak amplitudes of every particle, along with the particle transit time through the laser beam and the arrival time of each particle. It also digitizes and records signal and qualifier waveforms at a 40-MHz sample rate. The resulting time series of both the signal and qualifier waveforms may be viewed in postprocessing (viewed as if a high-speed digital oscilloscope were probing the signal and

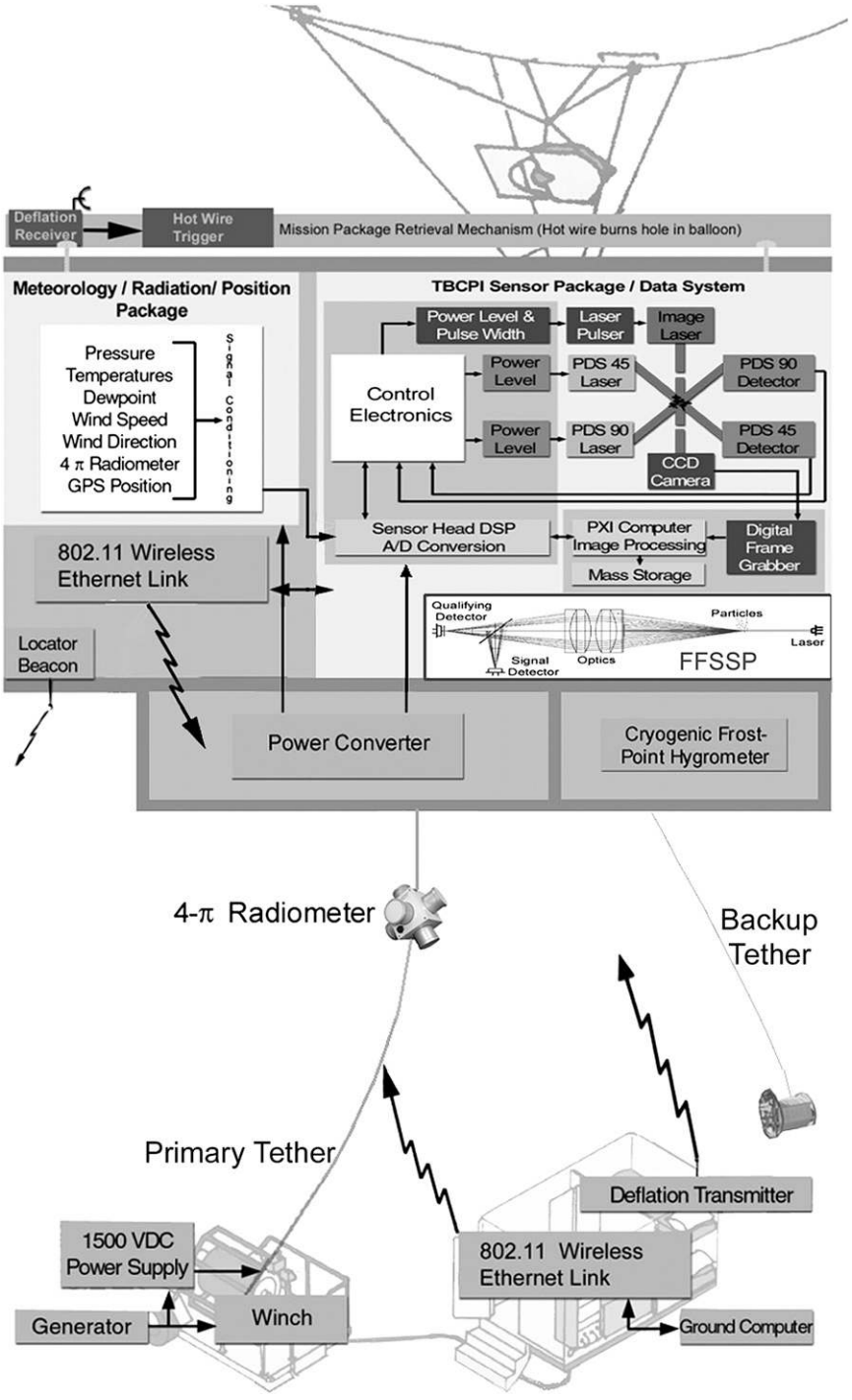

FIG. 2. Schematic illustration showing the principal components of the tethered-balloon system.

qualifier channels in real time). Analysis of the recorded waveforms reveals characteristics of noise, coincident particles, and other error signals that may be used to improve data-processing algorithms.

The 4-π radiometer measures hemispherical irradiances normal to each of its six faces at both 500 and 800 nm. As shown in Fig. 1, the 4-π radiometer is cube shaped, with 20-cm dimensions per side. It weighs 1.42 kg, including the combination power and data cable. It operates from a 12-Vdc supply, drawing a maximum of 200 mA. Six sensors, mounted on each side of the cube, measure the directional dependence of the radiation

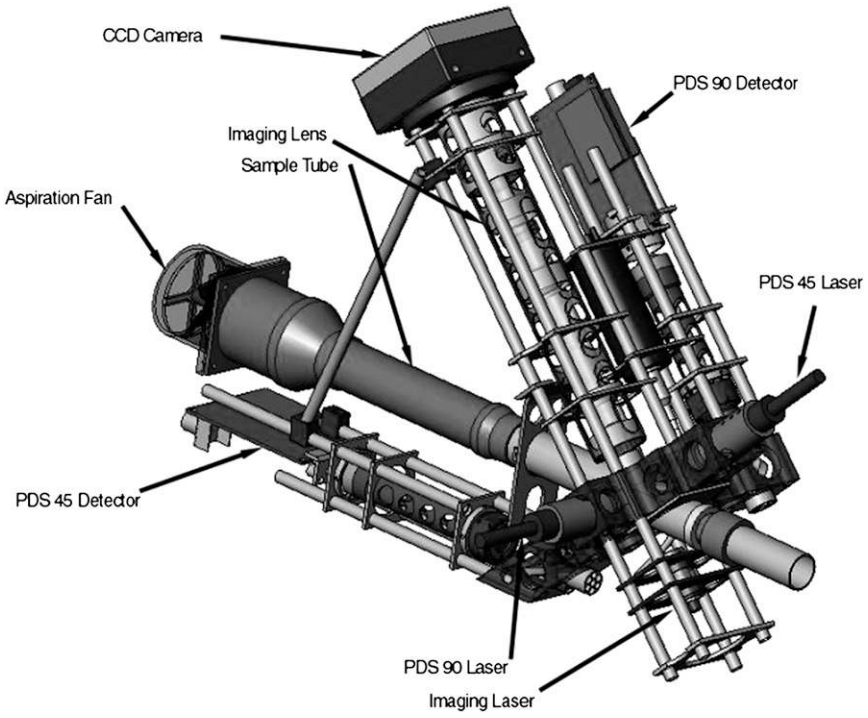

FIG. 3. Solid model showing the principal components of the TBS CPI.

field. Signals from the 4-π radiometer are interfaced directly to an RS-232 serial port on the meteorological data acquisition single-board computer (SBC). Software queries the radiometer for data once per second and combines the data stream with a data stream put together from readings of the other meteorological sensors. The data stream thus formed is sent from the SBC to the main data computer via another RS-232 link. Each radiation sensor has two photodiode detectors situated behind a diffuser and a filter; the filter response curves have approximate bandwidths of 10 nm. By subtracting radiation readings from opposite sides, a direct measure of the irradiance is obtained, while the sum of the radiation measurements is proportional to the mean intensity.

Measuring the mean intensity has several advantages over measuring horizontal hemispherical irradiances:

(i) no leveling of the instrument is required, there is just a sensor with isotropic response;
(ii) it completely circumvents several familiar problems associated with measurements of the net irradiance and its divergence, such as 1) the subtraction of downwelling and upwelling hemispherical fluxes to obtain the net flux, 2) the subtraction (finite differencing) of net fluxes to obtain the flux divergence, and 3) the imperfect cosine response of the instrument, which is the most severe at high latitudes where low solar elevations prevail;
(iii) the mean intensity is summed over all directions and its measurement suffers from none of the limitations enumerated above for hemispherical flux;
(iv) under cloudy situations, the horizontal hemispherical fluxes and the derived divergence lose significance unless the cloud is perfectly ''plane parallel,'' a situation that almost never occurs; and
(v) even if the leveling problem is ignored, the mean intensity, measured from an airborne platform, is much more sensitive to changes in surface albedo than the upward irradiance measured with a downward-looking irradiance sensor mounted on the platform.

Because of the value of the instrument package, we elected to use a second (backup) tether that is made of Vectran and is much lighter than the powered tether. In the unlikely event that the primary tether (with a 580-lb breaking strength) and the backup (with a 750-lb breaking strength) tether both break, a radio signal is sent from the ground that activates a deflation mechanism. Upon activation, a battery pack heats a nichrome wire that burns into the top of the balloon, allowing it to deflate and slowly descend. The instrument package has a battery-powered radio beacon that continues to transmit a directional signal so that the balloon and package can be located in the unlikely event that both the primary and backup tether were to break.

The 43-m^3 balloon has been operated safely at wind speeds of up to about 15 m s^{-1}, but maximum safe operating wind speeds may be less due to wind shear and turbulence near the ground. Also, higher wind velocities decrease the angle between the tether and surface, so that more tether is needed to gain an equivalent elevation in a no-wind condition. The increased ratio of tether length to elevation gain results in a lower maximum altitude. The balloon can be overinflated to achieve increased elevation. The manufacturer (The Blimpworks, Inc.; see http://www.theblimpworks.com) states that the balloon can be overinflated by up to 50%, but we have only overinflated it by about 10%–20% during our deployments at Svalbard and the South Pole. Because the balloon expands when overinflated, it increases the amount of air that is displaced by helium and therefore increases the lifting capacity of the balloon. However, if the balloon is inflated to the point where it stops expanding as helium is added, then the balloon actually starts loosing lift because the helium becomes more concentrated and increases the weight of the balloon (i.e., the helium is not at ambient pressure).

The balloon is rigged to produce zero aerodynamic lift. The balloon could be rigged to be a lifting body, which would theoretically increase its elevation as a function of increasing wind speed; however, this approach has not been tested. In high-wind regimes that prohibit balloon operation, the instrument package could be lofted either by using a tethered kite (Balsley et al. 1998) or by a balloon that is designed especially for high winds (e.g., see http://www.skydocballoon.com), which has been demonstrated to operate in winds exceeding 30 m s^{-1}. Because of the design of the SkyDoc balloon, its maximum achievable altitude is about 1 km. Deployment of the tethered-balloon package in Ny-Ålesund during May 2008 resulted in over 70 h of data collection in icing conditions with temperatures ranging from about 0° to −10°C. A scraper on the winch automatically shaves any accumulated rime ice from the tether when the balloon is lowered during vertical profiling.

3. Examples of data collected with the TBS at Ny-Ålesund and the South Pole

The TBS was deployed at the Ny-Ålesund research station (79°N) from 4 May through 2 June 2008. Table 1 lists the dates, times, and comments for each balloon flight. Ny-Ålesund was surrounded by open water during the entire field deployment. As seen in Table 1, the clouds were mostly mixed phase. The temperature range sampled by the TBS package while in cloud ranged from +2° to −8°C. On occasion, the TBS package penetrated through the cloud top prior to reaching its maximum altitude of about 1.6 km, so these mixed-phase clouds sometimes existed when cloud-top temperatures were warmer than −8°C. However, there was no way to verify the absence of higher clouds from which ice crystals could have seeded the lower clouds. In some cases such seeding was highly unlikely, because the low stratus cloud was composed of all water drops above ice particles. Figure 4 shows an example of CPI images and measurements from the 4-π radiometer that were collected on 29 May 2008 in a cloud that contained water drops above ice particles. The observation that there was a layer of water drops above ice particles suggests that the ice in this cloud was not formed by ice falling from higher clouds. Another highly unusual feature of these measurements is that the ice particles just above the cloud base were observed in a temperature range from about −1° to −3°C. Ice formation within this relatively warm temperature range is rare. Although there is no confirmatory evidence for the observation of ice particles forming at cloud base and not higher in the cloud, it is interesting to note that the location of the balloon launch is only a few hundred meters from a petroleum-fuel power plant.

The radiometric measurements in Fig. 4 show that, from about 1100 to 1215 UTC, when the radiometer was in the water cloud, the 500- and 800-nm channels measure irradiances of about 400 and 200 mW m^{-2} nm^{-1}, respectively. From about 1215 to 1300 UTC the radiometer is lowered into the ice region of the cloud and both channels measure 50–100 mW m^{-2} nm^{-1} less irradiance. This can be explained by the region of cloud drops above, where multiple scattering diffuses incoming solar radiation and decreases the irradiance measured in the ice cloud. During the time period from about 1330 to 1400 UTC the TBS ascended through cloud top and was exposed to direct sunlight. During this period, as expected, both the 500- and 800-nm irradiances increase sharply.

On 7 May 2008 the balloon ascended through a mixed-phase cloud that contained alternating layers of mostly ice and mostly supercooled cloud drops. Figure 5 shows representative CPI images arranged in a vertical profile. Figure 6 shows the effective particle diameter (D_{eff}) plotted as a function of height. For water drops D_{eff} is equal to the image maximum dimension, which is drop diameter, assuming that the drop is spherical. For ice particles D_{eff} is computed by dividing particle volume by particle area and multiplying the result by 2 times 0.75. Particle area is simply the projected area of the two-dimensional particle image, computed by adding all of the areas of the individually shaded pixels. Particle volume is determined using the technique described in Baker and Lawson (2006b), which uses an empirical formula

TABLE 1. List of TBS flights conducted at Ny-Ålesund.

Date (2008)	Begin time (UTC)	End time (UTC)	Max altitude (m AGL)	Temp range (°C)	Comments
4 May	1634	2023	1470	+2 to −10	Test fight (clear air)
5 May	0718	0908	770	−4 to −7	Test flight
6 May	0836	1651	883	+4 to −4	Test flight
7 May	0826	1219	1320	0 to −8	Mixed phase and all ice in upper cloud
12 May	1604	2305	1500	0 to −9	Mixed phase
13 May	1407	1502	869	0 to −6	Test flight
14 May	0723	1415	1376	−1 to −9	Mixed phase and mostly water–ice near ground
16 May	0810	0947	1399	0 to −7	Mixed phase
21 May	1207	1426	770	−2 to −8	Water cloud
22 May	1243	2041	939	+3 to −5	Mixed phase and mostly water
23 May	0914	1721	1600	+3 to −6	Water cloud
25 May	1200	1727	1214	+3 to −3	Mixed phase and mostly water
26 May	1055	1419	1061	+4 to −6	Mixed phase and heavy snow on ground
27 May	0831	1809	1370	+3 to −6	High clouds and longest-duration flight
29 May	1045	1525	1265	+1 to −4	Water over ice
2 Jun	1254	1413	1163	+5 to −2	Warm mixed phase (rain at the surface)

that incorporates particle maximum dimension, maximum transverse dimension, projected area, and perimeter. The black lines in the plots are the means of the size measurements averaged vertically over a fixed number of particles in order to better reveal the tendencies in the measurements. The averaging technique also better represents the vertical averaging that is inherent in remote retrievals. As a result of averaging water drop regions above and below regions with nearly clear air, the mean value line does not pass through the data points on the plot (e.g., the region near 650 m in Fig. 6). The main result of the data in Fig. 6 is that, compared with the all-ice regions, D_{eff} decreases in size rapidly in the mixed-phase regions of polar stratus clouds. The effect of cloud drops on D_{eff} will have a strong influence on the cloud radiative properties (Sun and Shine 1994). The ability of the TBS CPI to identify ice particles and cloud drops during vertical profiles can be used to improve microphysical retrievals using radiative transfer codes.

The CPI ice particle images observed on 7 and 29 May 2008, along with larger aggregates of ice crystals seen at the surface, are typical of those observed during the field deployment at Ny-Ålesund. Riming was generally observed on columns, sheaths, and needles that typically form at the relatively warm cloud temperatures (from 0° to about −10°C) investigated at Ny-Ålesund in May. Many of the ice particles had irregular shapes that could not be classified as classic hexagonal ice crystals, which agrees with the aircraft observations of ice particles in stratus clouds (Korolev et al. 1999).

The TBS was deployed to South Pole Station (SPS) for 12 days in January–February 2009 (Table 2). The ice surface at SPS is 2.8 km MSL and the surface temperature in January averaged about −30°C. Because of the much colder temperature at SPS compared to Ny-Ålesund, the winch was operated in a heated shack. Several other TBS operations had to be modified and safety precautions to personnel were taken due to the extreme cold.

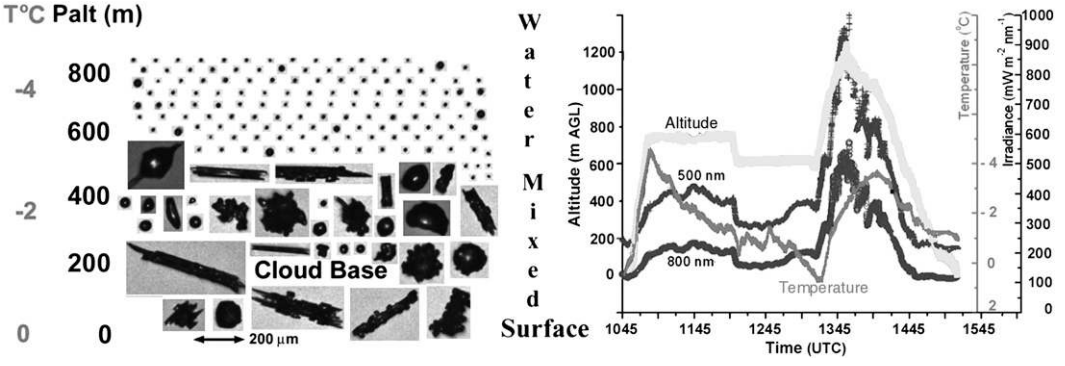

FIG. 4. Examples of (left) CPI images of crystals and water drops and (right) plot of altitude, temperature, and mean intensities obtained from the 4-π radiometer during a TBS ascent on 29 May 2008 at Ny-Ålesund.

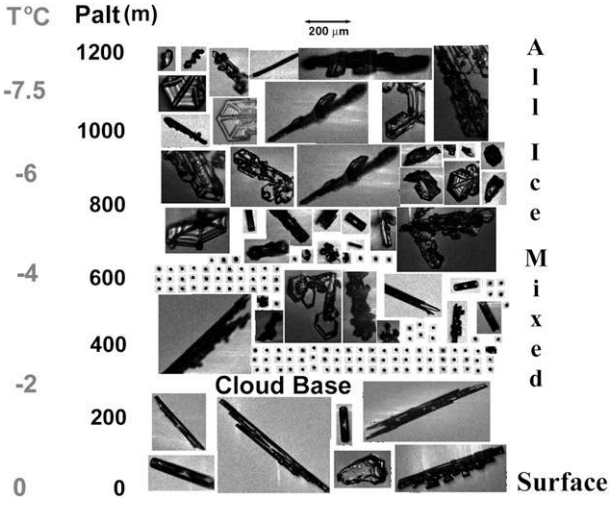

FIG. 5. Example of CPI images observed by the TBS on 7 May 2008 at Ny-Ålesund.

However, the instrument package operated normally and there were no major impediments to either the personnel or operations. Figure 7 shows photographs of the TBS camp at the South Pole.

In contrast to the predominance of irregularly shaped ice observed at Ny-Ålesund, CPI images of ice particles at SPS within the temperature regime from about −26° to −34°C often revealed ice crystals with hexagonal shapes. Some of the observations of hexagonally shaped ice particles occurred in mixed-phase clouds at very cold temperatures. For example, on 26 January 2009 the TBS ascended and descended through a mixed-phase cloud with predominantly hexagonally shaped ice particles and cloud drops at cloud top. Figure 8 shows a vertical profile of temperature and representative CPI images observed by the TBS. The temperature ranged from about −30° to −32°C in this cloud, which is much colder than any of the clouds observed at Ny-Ålesund. Also, the cloud was composed of nearly all water drops near cloud top at −32°C. A noticeable difference in the Ny-Ålesund and SPS ice crystal images (cf. Figs. 4 and 8) is the lack of riming on the large majority of ice crystals that coexisted with supercooled water at SPS. Based on CPI imagery in wave clouds, Baker and Lawson (2006a) found that the riming threshold for columns was 56–81 μm, which is consistent with the earlier work of Ono (1969), who reported a riming threshold of 50–90 μm. As seen in Fig. 8, only a few of the columns approach the riming threshold size. In contrast, CPI images collected in mixed-phase cloud at SPS on 1 February 2009 (Fig. 9) grew to larger sizes and were much more rimed, as were the crystals at Ny-Ålesund (Fig. 4). A curious aspect are the pristine ice crystals seen near the surface in the left panel of Fig. 9, and below the layer of supercooled water extending to the surface in Fig. 8 and the right panel of Fig. 9. Based on the measurements, it is not possible to determine whether these crystals fell unrimed from the mixed-phase cloud or were nucleated below cloud via vapor deposition.

Figure 10 shows a plot of D_{eff} versus altitude in the same format as that of Fig. 6. Similar to the Ny-Ålesund data shown in Fig. 6, D_{eff} decreases dramatically in the mixed-phase and all-water portions of cloud. The maximum particle size in the mixed-phase Antarctic cloud is noticeably smaller than the clouds at Ny-Ålesund,

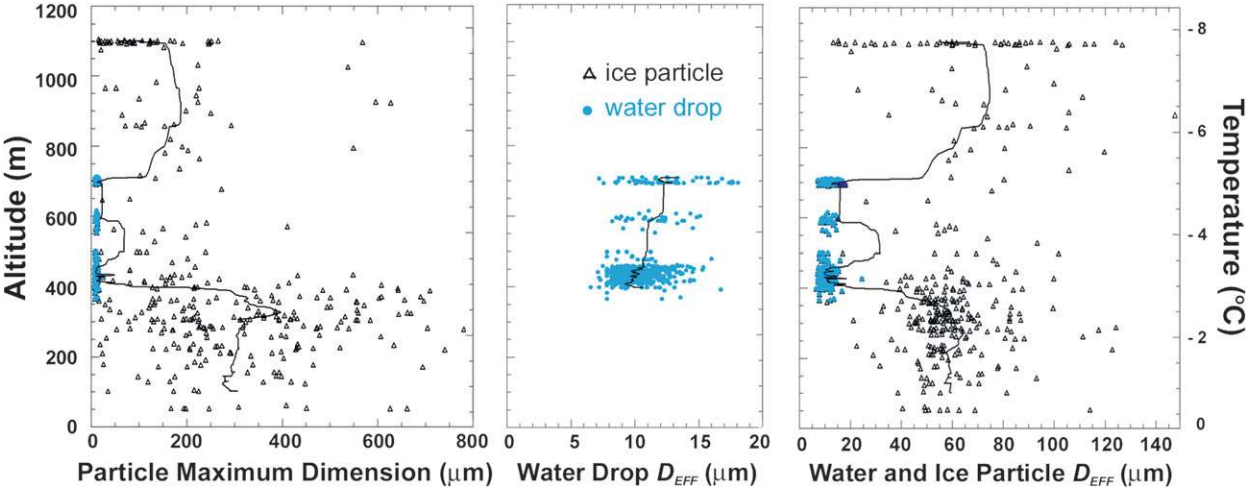

FIG. 6. (left) Maximum particle dimension as a function of altitude from sea level (equal to AGL) obtained from CPI images by separating ice particles (triangles) and water drops (blue dots). (middle) Effective water drop diameter (D_{eff}) vs altitude. (right) Ice particle (D_{eff}) and water drop (D_{eff}) plotted vs altitude. Data collected by TBS on 7 May 2008 at Ny-Ålesund.

TABLE 2. List of TBS flights conducted at the South Pole.

Date (2009)	Start time (UTC)	End time (UTC)	Max altitude (m AGL)	Temp range (°C)	Particle type/notes
23 Jan	0211	0401	490	−28 to −32	Bullets, rosettes, and columns
25 Jan	0022	0526	550	−29 to −33	Plates and columns, rosettes
26 Jan	0215	0528	500	−29 to −32	Mixed phase, columns, and plates
27 Jan	0332	0530	400	−28 to −31	Plates and columns
28 Jan	0240	0450	153	−28 to −30	Plates and columns
29 Jan	0000	0545	460	−27 to −29	Plates and columns
30 Jan	0139	0443	430	−29 to −31	Plates, columns, and bullets
31 Jan	0030	0508	700	−29 to −32	Rosettes, columns, and aggregates
1 Feb	0140	0310	520	−29 to −31	Mixed phase and rimed irregulars
1 Feb	0342	0442	540	−29 to −31	Mixed phase and lightly rimed columns
2 Feb	0256	0456	490	−28 to −30	Rosettes and bullets
2 Feb	2237	2407	580	−30 to −36	Rosettes and bullets
3 Feb	0222	0512	640	−30 to −34	Rosettes and bullets

which is expected because of the slower ice growth and aggregation rates at the much colder temperatures (see Pruppacher and Klett 1997). The presence of water drops at −32°C is not expected and is generally not included in polar models of radiative transfer. The National Aeronautics and Space Administration (NASA) Micro-Pulse Lidar Network (MPLNET) has operated a micropulse lidar (MPL; Spinhirne et al. 1995) at SPS since 1999 under a cooperative arrangement between NASA and the National Oceanic and Atmospheric Administration (NOAA), with support from the National Science Foundation (NSF). MPLNET lidar description and level 1 data are described by Campbell et al. (2002) and Welton and Campbell (2002). Figure 11 shows the backscatter return of the SPS MPL, which is vertically pointing and located about 300 m from the TBS launch site, during the period when the TBS was sampling the mixed-phase cloud represented in Figs. 8 and 10. The mixed-phase cloud is much denser optically than the ice cloud base and it is characterized by the strong signal between 3.325 and 3.4 km MSL. The SPS MPL signal below about 3.25 km is considered unusable because of level 1 overlap correction (Campbell et al. 2002). Using the pattern shown in Fig. 11 as an indicator, we anticipate conducting a climatological study of data from the SPS MPL to shed light on the frequency of mixed-phase clouds over the Antarctic Plateau.

4. Summary and future developments of the TBS

The tethered-balloon system (TBS) is shown to be a viable platform for cloud physics and radiation measurements in polar stratus clouds. The TBS has advantages and disadvantages over research aircraft platforms, which are summarized in the introduction of this paper. The TBS was deployed at Ny-Ålesund (79°N) for a 30-day period and at South Pole Station (SPS) for 10 days. The TBS reached altitudes of 1.6 km MSL at Ny-Ålesund and 800 m MSL at SPS. The maximum altitude difference is partially due to the SPS instrument package being about 2 kg heavier than that at Ny-Ålesund, but is also due to the 2.8-km SPS surface level compared to the sea level at Ny-Ålesund. The temperature ranged from about +2° to −9°C in the clouds investigated at Ny-Ålesund and from −27° to −34°C in the clouds at SPS. Mixed-phase clouds were predominant at Ny-Ålesund and were also observed at SPS on 2 of the 10 days at SPS; however, while mixed-phase clouds may have been present more often at SPS, no attempt was made to sample all of the clouds on all of the days.

The TBS CPI performed very well and appears to be an excellent instrument for distinguishing water drops from ice particles, and in determining ice particle shape (i.e., crystal habit) and the degree of crystal riming. The CPI and PC-based data acquisition system weighed 7 kg. A much lighter (2 kg) version of the CPI, which incorporates a fast FSSP in the particle detection optics, has been developed by SPEC for application on small, unmanned aerial vehicles (UAVs) and tethered balloons. The combination micro-CPI/FSSP was flown on the TBS at SPS, but the CPI component of the instrument was not operational.

An outstanding issue associated with the use of a TBS CPI to make quantitative particle size distribution measurements is that the particle collection efficiency is a function of particle size and ambient wind speed. When a CPI is mounted on an aircraft, the speed of the aircraft (say 100 m s^{-1}) is much faster than the fall velocity of the largest particles that the CPI images (about 1 m s^{-1} for a 1-mm particle). Thus, in an airborne application, if one neglects other effects such as particle sorting resulting from airflow effects, all of the particles have about the same probability of entering the sample volume. In

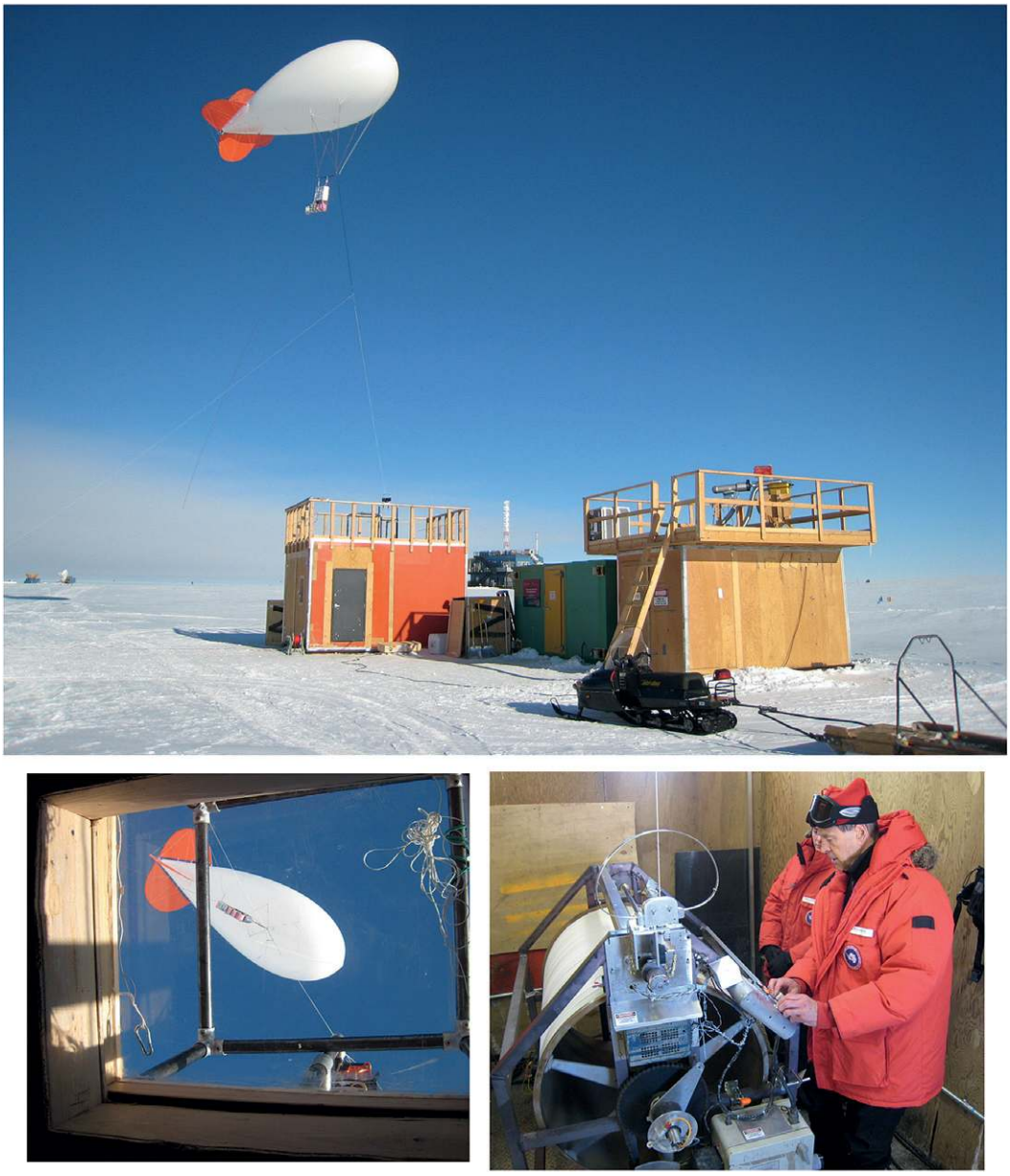

FIG. 7. Photographs. (top) The TBS camp at SPS. (bottom right) The building with the orange walls housed the winch.The tether passed through a custom portal in the ceiling and was directed using a swivel and pulley system installed on a gantry on the roof. (bottom left) A skylight that allowed the operator to view the balloon. (top) The top of the NOAA/Atmospheric Research Observatory and tower are visible (about 300 m in the background) between the orange and turquoise buildings.

contrast, the TBS system uses a fan to aspirate the sample volume, and the actual flow through the sample tube is a function of the ambient wind speed and the fan aspiration.

Because cloud drops have a fall velocity of a few centimeters per second and ice particles hundreds of microns in size fall at speeds on the order of hundreds of centimeters per second, the sample tube has to be oriented toward the vertical in order to capture the larger ice particles. However, if the sample tube is oriented straight up, then in a moderate wind situation, some of the cloud drops may blow by or impact the sample tube instead of being drawn down through the sample volume. SPEC plans to perform computational fluid dynamics (CFD) modeling of the flow around the balloon, instrument package, and inlet tube to estimate the collection efficiencies of

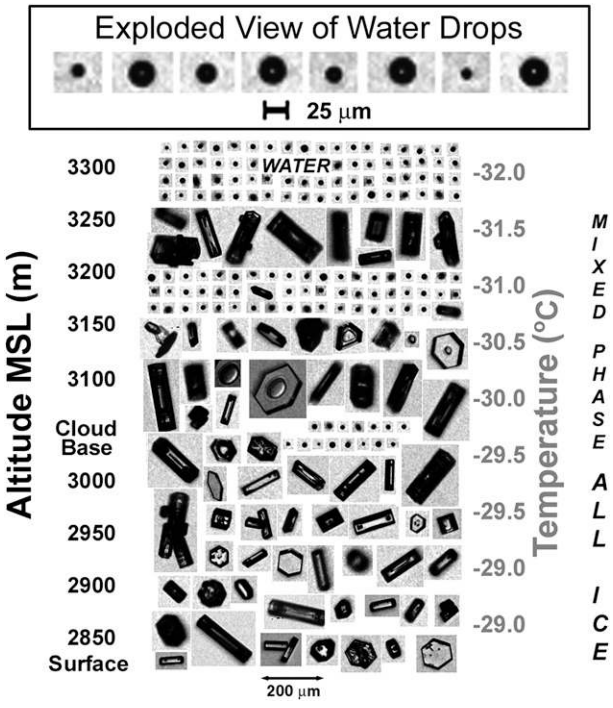

FIG. 8. As in Fig. 5, but for CPI images that were collected at the South Pole on 26 Jan.

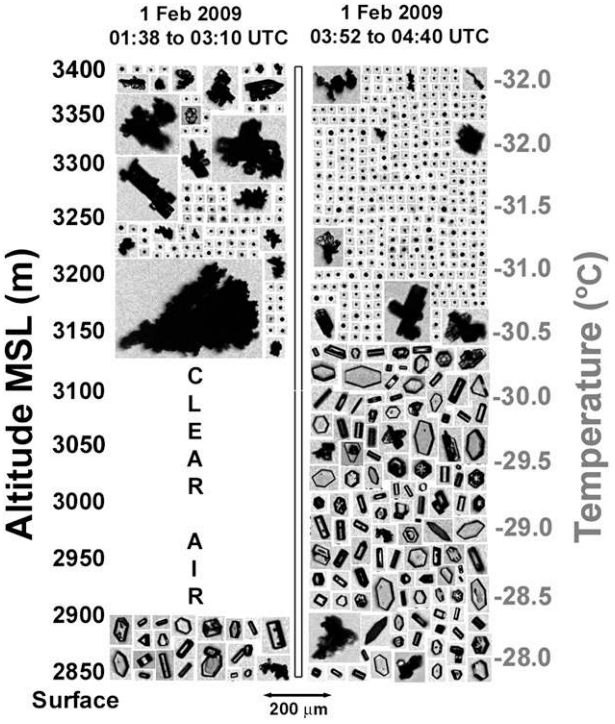

FIG. 9. As in Fig. 8, but the for the images that were collected on 1 Feb 2009.

various particles under various ambient conditions. To make quantitative estimates of particle size distributions with a TBS, the CFD results will need to be combined with measurements of aspirated airflow rate within the sample tube under various ambient wind conditions.

Based on preliminary results from the Ny-Ålesund field campaign, the 4-π radiometer appears to be a valuable instrument for measuring actinic flux (Stamnes and Storvold 1999; Sikand et al. 2010). In this paper only qualitative 4-π measurements were shown to demonstrate the viability of the instrument. Because the TBS can obtain vertical profiles within clouds, it presents a more representative view of the cloud properties observed by vertically pointing ground-based and airborne remote sensors. Future data analyses that combine the microphysics and radiation measurements may lead to improved remote retrieval algorithms and parameterizations used in column models.

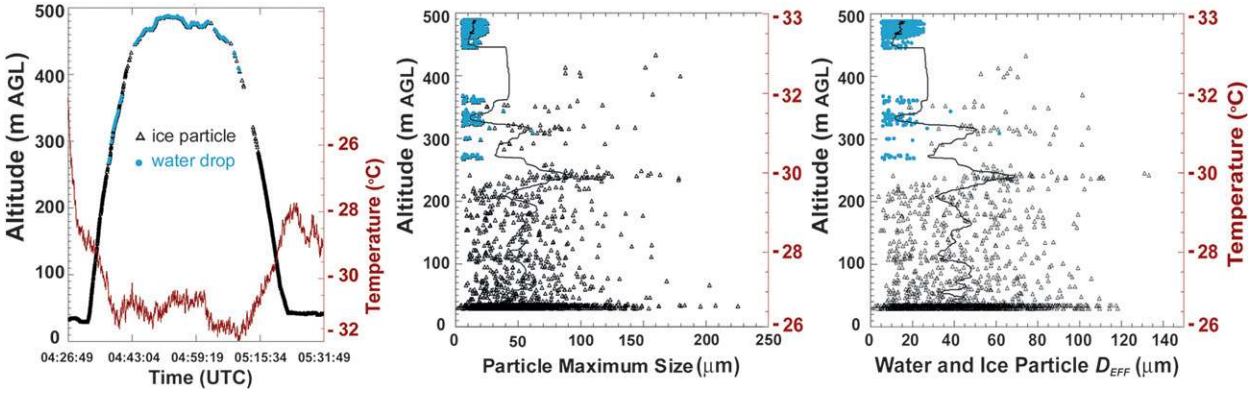

FIG. 10. (left) Time series plot of altitude (black line referenced to left ordinate) and temperature (magenta line referenced to right ordinate). (middle) Maximum particle dimension as a function of altitude obtained from CPI images by separating ice particles (triangles) and water drops (blue dots). (right) Ice particle (D_{eff}) and water drop (D_{eff}) plotted vs altitude. Data collected by TBS on 26 Jan 2009 at the South Pole.

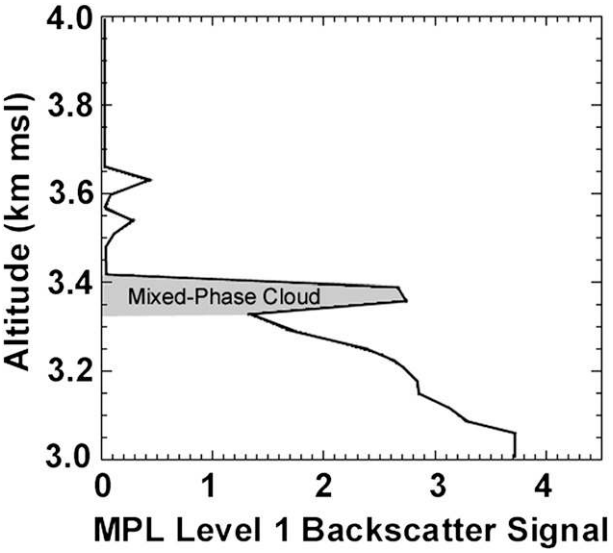

FIG. 11. Plot showing the vertical profile of the NASA level 1 backscatter response of a MPL at the South Pole on 26 Jan 2009. The identification of mixed-phase cloud is based on analysis of CPI imagery and the understanding that lidar backscatter is much stronger when relatively high concentrations of water drops are present, compared with low concentrations of ice particles.

Results from the Ny-Ålesund and South Pole demonstration projects presented in this paper show that the TBS is a valuable platform for making microphysical and radiometric measurements in polar stratus clouds. The TBS is unique in that it can make vertical profiles of clouds without disturbing the cloud environment. However, quantification of particle size distributions is a work in progress and requires additional dynamic calibration efforts. The two field projects described here have led to significant advances in our understanding of the assets and challenges of deploying a TBS in a polar environment. However, TBS technology is in its infancy and needs much more testing and the support of the scientific community before it becomes a turnkey operation with quantifiable results.

Now that the TBS has demonstrated its value as a tool for making cloud measurements, it has been suggested that several new, small instruments be incorporated into the package. Aerosol instruments, such as a cloud condensation nuclei (CCN) counter and ice nuclei filters are available. Also, small lidars can be incorporated into the package, as well as infrared radiometers and a host of other sensors. The 43-m^3 balloon is barely adequate to support the existing instrumentation, so larger balloons are anticipated for use in future projects. One likely candidate can lift twice the payload of the current balloon. The future of tethered-balloon measurements will depend on recognition of its value and the level of support provided by the scientific community.

Acknowledgments. We thank the Raytheon Polar Services Corporation staff at the South Pole, especially Al Baker and Paul Sullivan, along with too many others to mention, for their excellent support of our project. They were available and up to the task of providing support for a novel and challenging logistical project. We appreciate the participation of Alexei Korolev, especially for several lively discussions at the South Pole. At Ny-Ålesund we received excellent logistical support from Kings Bay, Ltd. We thank Børge Hamre and Lars Burkhardt from the University of Bergen, and Trond Svenøe of the Norwegian Polar Institute for their enthusiastic help with the Ny-Ålesund project. The South Pole Project was supported by National Science Foundation Office of Polar Programs Grant OPP-0337876 to SPEC. MPLNET is funded by the NASA Earth Observing System and Radiation Sciences Program, and the SPS MPLNET site is maintained with support from NOAA and the NSF Office of Polar Programs. A portion of the balloon instrument package was funded through NASA Contract NNG05CA06C. The Ny-Ålesund project was supported by the National Science Foundation Physical Meteorology Program Grant ATM-0752893 to Stevens Institute of Technology, and by the Norwegian Research Council through its International Polar Year program and the IPY-THORPEX project (Grant 175992/S30; http://www.ipy-thorpex.no).

REFERENCES

Alley, R. B., 1995: Resolved: The Arctic controls global climate change. *Arctic Oceanography: Marginal Ice Zones and Continental Shelves,* W. O. Smith and J. M. Grebmeier, Eds., Coastal and Estuarine Studies, Vol. 49, Amer. Geophys. Union, 263–283.

Arzel, O., T. Fichefet, and H. Goosse, 2006: Sea ice evolution over the 20th and 21st centuries as simulated by current AOGCMs. *Ocean Modell.,* **12,** 401–415.

Baker, B. A., and R. P. Lawson, 2006a: In situ observations of the microphysical properties of wave, cirrus and anvil clouds. Part I: Wave clouds. *J. Atmos. Sci.,* **63,** 3160–3185.

——, and ——, 2006b: Improvement in determination of ice water content from two-dimensional particle imagery: Part I: Image to mass relationships. *J. Appl. Meteor. Climatol.,* **45,** 1282–1290.

——, A. Korolev, R. P. Lawson, D. O'Connor, and Q. Mo, 2009: Drop size distributions and the lack of small drops in RICO rain shafts. *J. Appl. Meteor. Climatol.,* **48,** 616–623.

Balsley, B. B., M. L. Jensen, and R. G. Frehlich, 1998: The use of state-of-the-art kites for profiling the lower atmosphere. *Bound.-Layer Meteor.,* **87,** 1–25.

Baumgardner, D., and A. Korolev, 1997: Airspeed corrections for optical array probe sample volumes. *J. Atmos. Oceanic Technol.,* **14,** 1224–1229.

——, J. E. Dye, R. G. Knollenberg, and B. W. Gandrud, 1992: Interpretation of measurements made by the Forward Scattering Spectrometer Probe (FSSP-300X) during the Airborne Arctic Stratospheric Expedition. *J. Geophys. Res.,* **97,** 8035–8046.

Borys, R. D., K. Stamnes, R. Storvold, and P. Lawson, 1999: Development and deployment of a powered tethered balloon system at the SHEBA ice camp for measurements of cloud micro-physical and radiative properties. *Proc. of the Arctic Forum 1999,* Fairbanks, AK, Arctic Research Consortium of the United States.

Brenguier, J.-L., T. Bourrianne, A. de Araujo Coelho, J. Isbert, R. Peytavi, D. Trevarin, and P. Wechsler, 1998: Improvements of droplet size distribution measurements with the fast-FSSP. *J. Atmos. Oceanic Technol.,* **15,** 1077–1090.

Campbell, J. R., D. L. Hlavka, E. J. Welton, C. J. Flynn, D. D. Turner, J. D. Spinhirne, V. S. Scott, and I. H. Hwang, 2002: Full-time, eye-safe cloud and aerosol lidar observation at atmospheric radiation measurement program sites: Instrument and data processing. *J. Atmos. Oceanic Technol.,* **19,** 431–442.

Chapman, W. L., and J. E. Walsh, 1993: Recent variations of sea ice and air temperatures in high latitudes. *Bull. Amer. Meteor. Soc.,* **74,** 33–47.

Chen, Y., J. A. Francis, and J. R. Miller, 2002: Surface temperature of the Arctic: Comparison of TOVS satellite retrievals with surface observations. *J. Climate,* **15,** 3698–3708.

Curry, J. A., and E. E. Ebert, 1992: Annual cycle of radiative fluxes over the Arctic Ocean: Sensitivity to cloud optical properties. *J. Climate,* **5,** 1267–1280.

Emanuel, K. A., and R. Rotunno, 1989: Polar lows as arctic hurricanes. *Tellus,* **41A,** 1–17.

Field, P. R., R. Wood, P. R. A. Brown, P. H. Kaye, E. Hirst, R. Greenaway, and J. A. Smith, 2003: Ice particle interarrival times measured with a fast FSSP. *J. Atmos. Oceanic Technol.,* **20,** 249–261.

Grønås, S., and P. Skeie, 1999: A case study of strong winds at an Arctic front. *Tellus,* **51A,** 865–879.

Heymsfield, A. J., and L. M. Miloshevich, 1995: Relative humidity and temperature influences on cirrus formation and evolution: Observations from wave clouds and FIRE II. *J. Atmos. Sci.,* **52,** 4302–4326.

Hogan, R., P. Francis, H. Flentje, A. Hollingsworth, M. Quante, and J. Pelon, 2003: Characteristics of mixed-phase clouds. I: Lidar, radar and aircraft observations from CLARE '98. *Quart. J. Roy. Meteor. Soc.,* **129,** 2089–2116.

Holland, M. M., and C. M. Bitz, 2003: Polar amplification of climate change in coupled models. *Climate Dyn.,* **21,** 221–232.

Houghton, J. T., Y. Ding, M. Noguer, P. J. van der Linden, X. Dai, K. Maskell, and C. A. Johnson, Eds., 2001: *Climate Change 2001: The Scientific Basis*. Cambridge University Press, 881 pp.

Intrieri, J. M., C. Fairall, M. Shupe, P. Persson, E. Andreas, P. Guest, and R. Moritz, 2002a: Annual cycle of Arctic surface cloud forcing at SHEBA. *J. Geophys. Res.,* **107,** 8039, doi:10.1029/2000JC000439.

——, M. D. Shupe, T. Uttal, and B. J. McCarty, 2002b: Annual cycle of Arctic cloud geometry and phase from radar and lidar at SHEBA. *J. Geophys. Res.,* **107,** 8030, doi:10.1029/2000JC000423.

Korolev, A. V., and G. A. Isaac, 2003: Roundness and aspect ratio of particles in ice clouds. *J. Atmos. Sci.,* **60,** 1795–1808.

——, and ——, 2005: Shattering during sampling by OAPs and HVPS. Part I: Snow particles. *J. Atmos. Oceanic Technol.,* **22,** 528–542.

——, ——, and J. Hallett, 1999: Ice particle habits in Arctic clouds. *Geophys. Res. Lett.,* **26,** 1299–1302.

Lawson, R. P., and P. Zuidema, 2009: Aircraft microphysical and surface-based radar observations. *J. Atmos. Sci.,* **66,** 3505–3529.

——, B. A. Baker, C. G. Schmitt, and T. L. Jensen, 2001: An overview of microphysical properties of Arctic clouds observed in May and July during FIRE ACE. *J. Geophys. Res.,* **106,** 14 989–15 014.

——, ——, P. Zmarzly, D. O'Connor, Q. Mo, J.-F. Gayet, and V. Shcherbakov, 2006: Microphysical and optical properties of ice crystals at South Pole Station. *J. Appl. Meteor. Climatol.,* **45,** 1505–1524.

Meehl, G. A., and W. M. Washington, 1990: CO_2 climate sensitivity and snow-sea-ice albedo parameterization in an atmospheric GCM coupled to a mixed layer ocean model. *Climatic Change,* **16,** 283–306.

Ono, A., 1969: The shape and riming properties of ice crystals in natural clouds. *J. Atmos. Sci.,* **26,** 138–147.

Orikasa, N., and M. Murakami, 1997: A new version of hydrometeor videosonde for cirrus cloud observations. *J. Meteor. Soc. Japan,* **75,** 1033–1039.

Pruppacher, H. R., and J. D. Klett, 1997: *Microphysics of Clouds and Precipitation*. Kluwer Academic Publishers, 954 pp.

Rangno, A. L., and P. V. Hobbs, 1983: Production of ice particles in clouds due to aircraft penetrations. *J. Climate Appl. Meteor.,* **22,** 214–232.

Rothrock, D. A., Y. Yu, and G. A. Maykut, 1999: Thinning of the arctic ice cover. *Geophys. Res. Lett.,* **26,** 3469–3472.

Schweiger, A., and J. R. Key, 1994: Arctic Ocean radiative fluxes and cloud forcing estimates from the ISCCP C2 cloud dataset. *J. Appl. Meteor.,* **33,** 948–963.

Serreze, M., and Coauthors, 2000: Observational evidence of recent change in the northern high-latitude environment. *Climatic Change,* **46,** 159–207.

Sikand, M., J. Koskulics, K. Stamnes, B. Hamre, J. J. Stamnes, and R. P. Lawson, 2010: Optical properties of mixed phase boundary layer clouds observed from a tethered balloon platform in the Arctic. *J. Quant. Spectrosc. Radiat. Transfer,* **111,** 1921–1930.

Spinhirne, J. D., R. Rall, and V. S. Scott, 1995: Compact eye-safe lidar systems. *Rev. Laser Eng.,* **23,** 112–118.

Stamnes, K., and R. Storvold, 1999: Development and deployment of a powered tethered balloon system at the SHEBA ice camp for measurements of cloud microphysical and radiative properties. *Proc. of the Ninth Atmospheric Radiation Measurement (ARM) Science Team Meeting,* San Antonio, TX, ARM, 1–7.

Stone, R., 1997: Variations in western arctic temperature in response to cloud radiative and synoptic-scale influences. *J. Geophys. Res.,* **102,** 21 769–21 776.

Sun, Z., and K. Shine, 1994: Studies of the radiative properties of ice and mixed-phase clouds. *Quart. J. Roy. Meteor. Soc.,* **120,** 111–137.

Tsay, S.-C., K. Stamnes, and K. Jayaweera, 1989: Radiative energy budget in the cloudy and hazy Arctic. *J. Atmos. Sci.,* **46,** 1002–1018.

Vavrus, S. J., 2004: The impact of cloud feedbacks on Arctic climate under greenhouse forcing. *J. Climate,* **17,** 603–615.

Vinnikov, K. Y., and Coauthors, 1999: Global warming and Northern Hemisphere sea ice extent. *Science,* **286,** 1934–1937.

Vömel, H., D. E. David, and K. Smith, 2007: Accuracy of tropospheric and stratospheric water vapor measurements by the cryogenic frost point hygrometer: Instrumental details and observations. *J. Geophys. Res.,* **112,** D08305, doi:10.1029/2006JD007224.

Walden, V. P., M. E. Ellison, R. E. Brandt, M. S. Town, S. R. Hudson, and R. M. Jones, 2005: Properties of super-cooled water

clouds over South Pole. Preprints, *Eighth Conf. on Polar Meteorology and Oceanography,* San Diego, CA, Amer. Meteor. Soc., 6.1. [Available online at http://ams.confex.com/ams/pdfpapers/87694.pdf.]

Walsh, J. E., and W. L. Chapman, 1998: Arctic cloud–radiation–temperature associations in observational data and atmospheric reanalyses. *J. Climate,* **11,** 3030–3045.

——, S. J. Vavrus, and W. L. Chapman, 2005: Workshop on modeling of the Arctic atmosphere. *Bull. Amer. Meteor. Soc.,* **86,** 845–852.

Welton, E. J., and J. R. Campbell, 2002: Micropulse lidar signals: Uncertainty analysis. *J. Atmos. Oceanic Technol.,* **19,** 2089–2094.

Zhang, T., S. A. Bowling, and K. Stamnes, 1997: Impact of the atmosphere on surface radiative fluxes and snow melt in the Arctic and subarctic. *J. Geophys. Res.,* **102,** 4287–4302.

Zuidema, P., and Coauthors, 2004: An Arctic springtime mixed-phase cloudy boundary layer observed during SHEBA. *J. Atmos. Sci.,* **62,** 160–176.